

## A plasma solenoid driven by an Orbital Angular Momentum laser beam

R. Nuter<sup>1</sup>, Ph. Korneev<sup>2</sup>, I. Thiele<sup>3</sup> and V. Tikhonchuk<sup>1</sup>  
 1 *Université Bordeaux, CNRS, CEA, UMR 5107, 33405 Talence, France* - 2 *National Research Nuclear University 'MEPhI', Moscow, 115409 Russian Federation, Lebedev Physical Institute, Moscow, 119333, Russian Federation* - 3 *Chalmers University of Technology, Department of Physics, SE-41296 Göteborg, Sweden*

A tens of Tesla quasi-static axial magnetic field can be produced in the interaction of a short intense laser beam carrying an Orbital Angular Momentum with an underdense plasma. Three-dimensional “Particle In Cell” simulations and analytical model demonstrate that orbital angular momentum is transferred from a tightly focused radially polarized laser beam to electrons without any dissipative effect. A theoretical model describing the ballistic interaction of electrons with laser shows that particles gain angular velocity during their radial and longitudinal drift in the laser field. The agreement between PIC simulations and the simplified model identifies routes to increase the intensity of the solenoidal magnetic field by controlling the orbital angular momentum and/or the energy of the laser beam.

The generation of a quasi-static magnetic field in the laser-plasma interaction is a subject of many theoretical [1–10] and experimental studies [11–13]. Two approaches are considered: one consists in designing the target in such way that the interaction with the laser generates controlled azimuthal currents [7, 8], another one proposes to transfer angular momentum from laser to electrons by using circularly polarized laser beam [1–6, 11–13] or laser beam with a structured spatial shape [9, 10]. In [1–6], the authors consider theoretically the magnetization of a medium exposed to a circularly polarized Gaussian laser beam. Plasma magnetization originates from the inverse Faraday effect, where the spin angular momentum of a laser beam is transferred to the plasma electrons due to dissipation processes such as collisions, ionization or radiation friction. This laser to electron angular momentum transfer has been experimentally observed [11–13]. Ali *et al.* [9], consider a linearly polarized laser beam carrying Orbital Angular Momentum (OAM) [14] and analytically demonstrate that such a laser beam transfers its OAM to electron through the inverse bremsstrahlung dissipative process. Léczy *et al.* [10] and Wang *et al.* [15] numerically model the interaction of a screw-shaped laser pulse with an underdense plasma and observe laser to electron OAM transfer in the laser wakefield.

In this letter, we demonstrate that a quasi-static axial magnetic field can be generated within a purely optical process, without any dissipative effects. It is produced in an underdense plasma irradiated by a radially polarized OAM laser beam, which is for example, experimentally designed by Li *et al.* [16]. The authors demonstrate their capacity to produce such laser beams with an energy ratio between radial and azimuthal components attaining 98%. Our three-dimensional (3D) Particle In Cell (PIC) simulations, modeling the laser-plasma interaction, clearly show an orbital angular momentum trans-

fer from laser to electron and the generation of a strong solenoidal magnetic field. A simplified model describing the laser-electron dynamics shows that this transfer originates from the joint radial and longitudinal electron motion in the laser field. The agreement observed between the 3D PIC simulations and the simplified model provides means for controlling the magnetic field with laser parameters.

To model a tightly focused radially polarized laser beam carrying OAM, we consider the numerical algorithm developed by Thiele *et al.* [17]. It consists in prescribing the temporal and spatial shape for the electromagnetic fields at the focal point  $x = x_0$  in vacuum, and then solving the Maxwell’s equations in vacuum to compute the electric and magnetic fields components at the box boundaries ( $x=0$  plane). This method provides the electromagnetic fields consistent with the Maxwell’s equations and is valid beyond the paraxial approximation for laser beam. The radially polarized OAM laser beam is prescribed at the focal point  $x = x_0$  in the cylindrical coordinates  $(r, \theta, x)$ :

$$\vec{E}(r, \theta, t, x_0) = E_0 \cdot g(t) \cdot f(r) \cos(l\theta - \omega_0 t) \cdot \vec{e}_r \quad (1)$$

with the radial distribution  $f(r) = C_l(r/w_0)^{|l|} e^{-(r/w_0)^2}$ , the temporal envelop  $g(t) = \cos^2(\pi \frac{t-t_0}{\tau})$  in the time interval  $|t - t_0| < \tau/2$ , the laser OAM  $l$ , the focal beam waist  $w_0 = 2 \mu\text{m}$ , the pulse duration  $\tau$  equal to 6 optical periods (T), the central time  $t_0$ , the laser amplitude  $E_0$ , the normalization factor  $C_l = \sqrt{2^{|l|+1}/|l|!}$  and the radial unit vector  $\vec{e}_r$ . The laser frequency  $\omega_0 = 2.3 \times 10^{15} \text{ s}^{-1}$  corresponds to the laser wavelength =  $0.8 \mu\text{m}$ . The electromagnetic energy distribution for the  $l = 1$  laser beam is illustrated in Fig. 1 (right panel). It is characterized by two entangled helices with electric field vectors directed along the same radial direction.

Interaction of such a laser beam with a collisionless

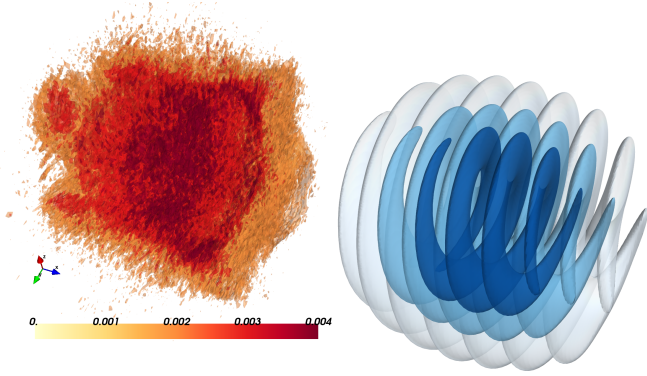


FIG. 1: (left) Solenoidal magnetic field  $B_x$  induced by an OAM  $l = 1$  laser beam, (right) helical energy distribution. The colormap applies to the  $B_x$  field.

underdense plasma is studied with the 3D PIC code OCEAN [18]. The numerical box is composed of 640 cells along the longitudinal axis  $x$ , and  $512 \times 512$  cells in the transverse plane  $(y, z)$ , with a spatial resolution of 19 nm. Absorbing conditions for the electromagnetic fields and particles are defined at the box boundaries. The laser pulse with an OAM  $l = 1$  and an intensity  $2 \times 10^{18}$  W/cm<sup>2</sup>, corresponding to the adimensionned field amplitude  $a_0 = eE_0/m_e\omega_0c = 1$  ( $m_e$  is the electron mass,  $e$  is the electron charge and  $c$  is the light speed in vacuum), is injected into the numerical box from the left border. The total laser energy is 2.5 mJ. The plasma composed of electrons and protons with an initial density equal  $1.74 \times 10^{19}$  cm<sup>-3</sup>, has a cylindrical spatial shape with a  $1.52 \mu\text{m}$  length and a  $6.9 \mu\text{m}$  diameter. Ten macro-particles per cell are considered.

From PIC simulations, we evaluate the averaged longitudinal orbital angular momentum gained by electron in the laser beam:

$$\langle L_x \rangle = \frac{1}{N_b} \sum_{i=1, N_b} w_i [(y_i - y_0) \times p_{z,i} - (z_i - z_0) \times p_{y,i}] \quad (2)$$

with the total number of electrons  $N_b$ , laser beam axis  $(y_0, z_0)$ , transverse coordinates  $(y_i, z_i)$  and transverse momenta  $(p_{y,i}, p_{z,i})$  of the macro-particle  $i$  defined with the weight  $w_i$ . Protons do not gain any significant angular momentum due to their mass 1836 times heavier than the electron's one. Solid curves in Fig. 2 display the temporal evolution of  $\langle L_x \rangle$ : the red and green curves, distinguishing electrons rotating in opposite directions, show a similar temporal behaviour but of an opposite sign. As the laser interacts with the plasma bulk, from  $\omega_0 t = 50$  to  $\omega_0 t = 100$  ( $1/\omega_0 = 0.4248$  fs), the absolute value of  $\langle L_x \rangle$  increases up to  $0.5 m_e c^2/\omega_0$ , and then decreases to a value close to  $0.15 - 0.2 m_e c^2/\omega_0$ . The black curve, displaying the total averaged electron angular momentum, exhibits a break around  $\omega_0 t \simeq 70$ .  $\langle L_x \rangle$  remains nonzero once the electron-laser interaction ends: equal to  $-0.08$

$m_e c^2/\omega_0$  at  $\omega_0 t \simeq 75$ , it slightly increases up to  $-0.063 m_e c^2/\omega_0$  at  $\omega_0 t \simeq 250$ . The dashed curves in Fig. 2, displaying the relative number of electrons with positive and negative angular momentum, show that the part of electrons with negative angular momentum continuously increases during their interaction with the laser. At the end of their interaction with the laser, more than 70% of electrons have acquired a negative angular momentum.

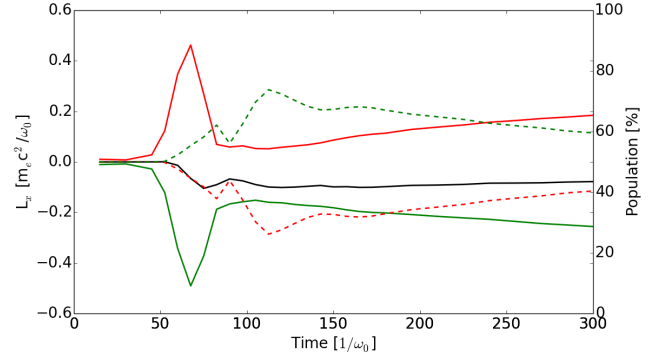


FIG. 2: Longitudinal orbital angular momentum averaged over all the electron population (black solid curve), over electrons with positive  $\langle L_x \rangle$  (red solid curve) and negative  $\langle L_x \rangle$  (green solid curve). Fraction of electron population with positive (red dashed curve) and negative (green dashed curve)  $\langle L_x \rangle$ .

The transversal cut of the electron longitudinal OAM distribution, shown in Fig. 3, displays a ring (a tube in 3D) containing the highest electron  $\langle L_x \rangle$  amplitude with an external radius  $r_1 \sim 15 c/\omega_0$  and an internal one  $r_0 \sim c/\omega_0$ . These rotating electrons, characterized by  $\langle L_x \rangle$  slightly lower than  $-0.4 m_e c^2/\omega_0$ , form a solenoidal structure with an axial magnetic field inside (left panel in Fig.1). The central hole shows electrons  $L_x$  close to zero values, in agreement with the laser intensity distribution.

The left panel in Fig. 1 displays an isocontour of the longitudinal magnetic field  $B_x$  once the laser has left the plasma area. The quasi-static  $B_x$  field presents a cylindrical shape: its axial length is equal to the plasma length ( $\sim 2.5 \mu\text{m}$ ) and its radius is limited by the contour where the laser intensity is maximal ( $r = 12 c/\omega_0$ ). The cylinder axis coincides with the laser one. The  $B_x$  maximal amplitude reaches  $0.004 m_e \omega_0/e$  (53 T).

We now compare this value with the  $B_x$  field generated by electrons localized in a hollow cylinder with a length  $l$ , an internal radius  $r_0$  and an external radius  $r_1$ . The electron density is set to  $n_e$  and the electron longitudinal orbital angular momentum is equal to  $l_x$ . We consider the laser unit system, where lengths are expressed in  $c/\omega_0 = 127.3$  nm, density is expressed in  $n_c = 1.74 \times 10^{19}$  cm<sup>-3</sup> (the plasma critical density) and magnetic field is expressed in  $B_c = m_e \omega_0/e = 13382$  Tesla. The derivation of the Biot-Savart law [19], pre-

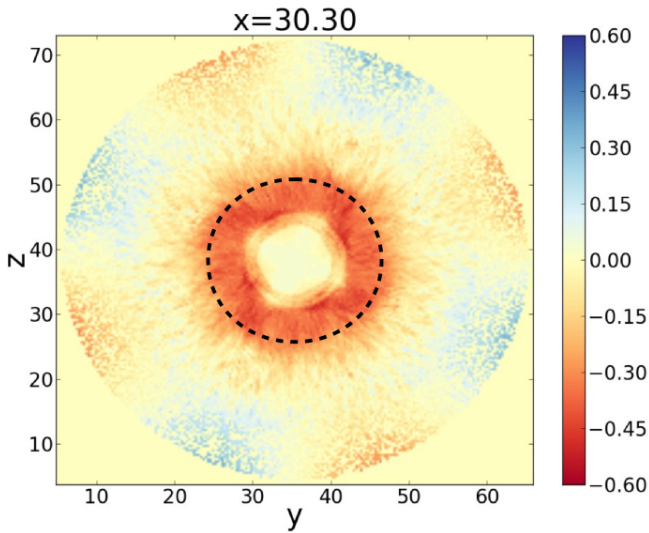


FIG. 3: Transversal cut of the electron  $L_x$  distribution near  $x = 30 c/\omega_0$  for  $\omega_0 t = 120$ . The dashed black curve displays the field maximum amplitude contour.

sented in the Supplementary Materials, results in

$$B_x \simeq -0.5 n_e l_x \left[ \frac{l}{r_0} - \frac{l}{r_1} \right] \quad (3)$$

Considering the values computed in PIC simulations:  $\langle L_x \rangle = -0.4 m_e c^2 / \omega_0$ ,  $n_e = 0.01 n_c$ ,  $l = 19 c / \omega_0$ ,  $r_0 = 6 c / \omega_0$  and  $r_1 = 15 c / \omega_0$ , we obtain  $B_x = 0.0038 B_c$  which perfectly agrees with the  $B_x$  value computed from PIC simulations and equal to  $0.004 B_c$ .

To understand how electrons gain their angular velocity, we have implemented in the OCEAN code a particle tracking module. This diagnostic consists in adding some arbitrarily chosen electrons that experience the electric and magnetic fields but do not produce the self-consistent fields, automatically computed in PIC simulations. Figure 4 displays the longitudinal OAM acquired by these “test electrons” at the end of their interaction with the laser beam as a function of their initial radial coordinate ( $r_0$ ), when the plasma motion is active (green circle) so that plasma self-consistent fields influence the laser-electron dynamics and when the plasma motion is “frozen” (gray markers) where these “test electrons” only experience the laser electromagnetic fields.

The green circles show that  $L_x$  values lower than  $-0.4 m_e c^2 / \omega_0$  are obtained for electrons initially localized in the zone where the laser intensity is maximum, i.e.  $r = 7 - 12 c / \omega_0$ . Moreover, the  $L_x$  spatial distribution follows the laser intensity spatial shape. Same characteristics are observed for the  $L_x$  radial distribution when the plasma motion is frozen (gray markers), except that the electron angular momenta reach higher absolute values. This demonstrates that the OAM transfer from laser beam to electrons is a pure optical process for which the

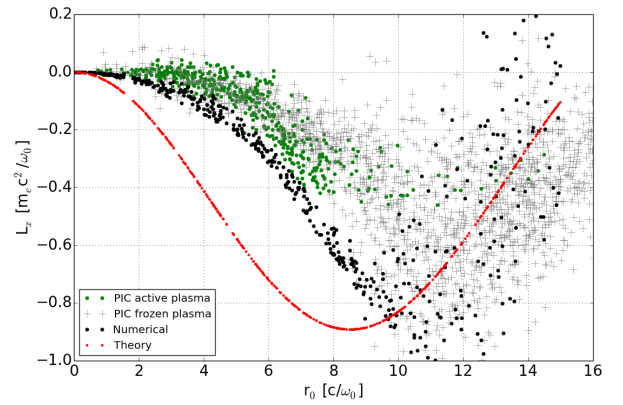


FIG. 4: Longitudinal orbital angular momentum ( $L_x$ ) computed at  $\omega_0 t = 97$  versus the initial electron radial position with (green circle) and without (gray markers) active plasma motion. The red dotted curve and the black circles display the  $L_x$  values computed, analytically and numerically, respectively, by using the perturbation theory.

efficiency is increased as the plasma self-consistent fields are turned off. When the plasma motion is active, a longitudinal charge separating field is generated on the rear plasma surface due to the ion inertia. This electrostatic field keeps the electrons confined in the plasma zone reducing their interaction time with the laser, and then their angular velocity gain.

Because these PIC simulations clearly highlight that the laser to electrons OAM transfer results from optical process only, we develop a reduced numerical model describing the laser beam induced electron dynamics. It solves the relativistic motion equations of an electron irradiated by the electric ( $E_r, E_\theta, E_x$ ) and magnetic fields ( $B_r, B_\theta, B_x$ ).

$$\dot{p}_r = -E_r - v_\theta B_x + v_x B_\theta + p_\theta \dot{\theta} \quad (4)$$

$$\dot{p}_\theta = -E_\theta - v_x B_r + v_r B_x - p_r \dot{\theta} \quad (5)$$

$$\dot{p}_x = -E_x - v_r B_\theta + v_\theta B_r \quad (6)$$

where  $p_r = \gamma v_r = \gamma \dot{r}$ ,  $p_\theta = \gamma v_\theta = \gamma r \dot{\theta}$  and  $p_x = \gamma v_x = \dot{x}$  are the radial, azimuthal and longitudinal electron momenta, respectively and  $\gamma = \sqrt{1 + p_r^2 + p_\theta^2 + p_x^2}$  is the Lorentz factor. As detailed in the Supplementary Materials, a radially polarized OAM laser beam is not an eigenmode of the Maxwell’s equations: it contains a small admixture of the azimuthal component out of the focal point. The electric and magnetic field components are

then approximated with :

$$E_r = a_0 f(r) g(t) \cos(\phi) \quad B_r = -la_0 \alpha f(r) g(t) \cos(\phi) \quad (7)$$

$$E_\theta = la_0 \alpha f(r) g(t) \cos(\phi) \quad B_\theta = a_0 f(r) g(t) \cos(\phi) \quad (8)$$

$$E_x = a_0 \frac{f(r)}{r} g(t) \sin(\phi) \quad B_x = -la_0 \frac{f(r)}{r} g(t) \cos(\phi) \quad (9)$$

where  $\phi = \omega_0 t - l\theta - x$  is the phase and  $\alpha \ll 1$  is the parameter accounting for the contribution of the additional azimuthal component generated out of the focal point. First, we assume a low laser intensity ( $a_0 \ll 1$ ) which allows a perturbative expansion of Eqs.(4, 5, 6) in powers of  $a_0$  (details are given in Supplementary Materials). Integrated over the pulse duration, the first order of electron OAM is zero, so that it does not contribute to the final electron OAM. The second order term of  $L_x$  solves :

$$\dot{L}_x^{(2)} = r^{(1)} \dot{p}_\theta^{(1)} - r_0 p_x^{(1)} B_r + r_0 p_r^{(1)} B_x - r_0 \frac{dE_\theta}{dr} (\vec{r}^{(1)} - \vec{r}_0) \quad (10)$$

In fact, only the  $-r_0 \frac{dE_\theta}{dr} (r^{(1)} - r_0)$  and  $-r_0 \frac{dE_\theta}{dx} (x^{(1)} - x_0)$  terms finally contribute to :

$$L_x^{(2)}(\tau) = -\alpha l a_0^2 f^2(r_0) \frac{3\tau}{8} \left[ 1 - \left( \frac{r_0}{w_0} \right)^2 \right] \quad (11)$$

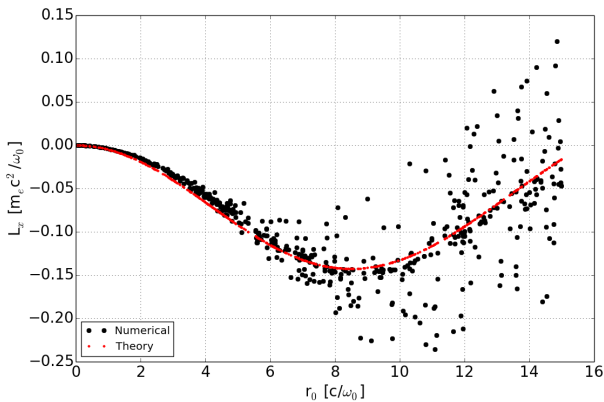


FIG. 5: Longitudinal orbital angular momentum of electrons versus their initial radial position computed from the numerical integration of motion equations (black circle) and the theoretical prediction according to Eq. 11 (red curve) for  $a_0 = 0.4$  and  $\alpha = 0.1$ . The other laser parameters are identical to the PIC simulations :  $w_0 = 2 \mu\text{m}$ ,  $\tau = 6 \text{ T}$ ,  $l = 1$ .

Figure 5 exhibits a perfect agreement between the electron  $L_x$  radial distribution computed from the numerical integration of Eqs.(4, 5, 6) and from the analytical expression (Eq.(11)) for  $a_0 = 0.4$ . As already observed in the PIC simulations [Fig. 4], even at low intensity, most

of the electrons acquire a negative longitudinal OAM. This analysis evidences that the laser to electron OAM transfer originates from the radial and longitudinal electron drift in the laser field. For  $r_0 = w_0/\sqrt{2}$  (where the intensity is maximum), the electrons acquire the maximum angular rotation, and the theoretical expression of  $L_x^{(2)}$  shows that the electron longitudinal motion contributes for 2/3 and the radial one for 1/3 to the final angular momentum value.

For higher laser intensity,  $a_0 = 1$ , the black circles and the red curve in Fig. 4 display the  $L_x^{(2)}$  values computed by numerically integrating Eqs. (4,5,6) and with the theoretical formula (Eq. (11)), respectively. The analytical expression deviates from the numerical integration of motion equations, but demonstrates a qualitative similar behaviour. We observe negative longitudinal OAM gained by electrons, and the correct order of magnitude for the  $L_x$  values. A relatively good agreement between numerical results and PIC simulations is evident even if the azimuthal component of the field is chosen constant along the laser propagation in the numerical model [see Supplementary materials for more details]. In both cases, the laser transfers to electrons negative  $L_x$  values, and the OAM transfer efficiency follows the laser intensity radial distribution.

The direction of the electron OAM changes by inverting the sign of the OAM laser beam [see Supplementary materials]. The generated solenoidal magnetic field is then directed to the opposite direction [see Fig.6(a)].

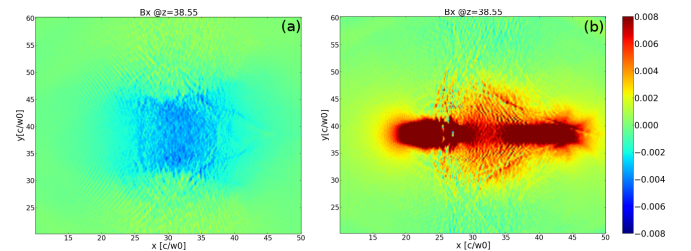


FIG. 6: Longitudinal cut of  $B_x$  computed from PIC simulations for  $l = -1$  and  $\tau = 6 \text{ T}$  (a) and  $l = 1$  and  $\tau = 12 \text{ T}$  (b). The others laser parameters are kept unchanged.

As suggested by Eq. (11), the electron OAM amplitude is higher as the pulse duration is increased [see Supplementary materials]. Figure 6(b), displaying the longitudinal cut of  $B_x$  computed with a pulse duration equal to 12 optical cycles, shows that its amplitude is two times higher than for a pulse duration equal to 6 optical cycles. The longitudinal extension of the magnetic field is larger than for the shorter pulse duration, because the electrons have acquired higher longitudinal momenta resulting in a larger plasma expansion.

In conclusion, we demonstrated that a tightly focused radially polarized laser beam is able to transfer its Orbital Angular Momentum to electrons without any dissipative

effects like collision or ionization. Only an optical process is responsible for the electron rotation gain, which originates from the radial and longitudinal electron drift in the laser field. Both radial and azimuthal components of the laser fields are needed for the laser to electron OAM transfer. By using 3D Particle In Cell simulations, we have shown that the rotated electrons produce a quasi-static magnetic field  $\sim 50$  T over more than 80 fs after the end of the laser-plasma interaction. This magnetic field is homogeneous over spatial dimensions (a  $2.5 \mu\text{m}$  length and a  $1.5 \mu\text{m}$  as transverse size) defined by the plasma length and the laser transverse size. An accurate choice of laser parameters, such as focal beam waist, laser intensity, laser OAM and/or pulse duration, make then possible a control of the quasi-static magnetic field production. A simple analytical model provides a quantitative estimation of the electron longitudinal orbital angular momentum values and the solenoidal magnetic field up to  $a_0 = 1$ . This work opens new ways to optically generate quasi-static magnetic field from the laser plasma interaction.

This work was granted access to HPC resources of TGCC under the allocation A0010506129 made by GENCI.

- 
- [1] V.I. Berezhiani, S.M. Mahajan, and N.L. Shatashvili. Theory of magnetic field generation by relativistically strong laser radiation. *Physical Review E*, 55:995, 1997.
- [2] Riccardo Hertel. Theory of the inverse Faraday effect in metals. *Journal of Magnetism and Magnetic Materials*, 303:L1, 2006.
- [3] G. Shvets, N.J. Fisch, and J.-M Rax. Magnetic field generation through angular momentum exchange between circularly polarized radiation and charged particles. *Physical Review E*, 65:046403, 2002.
- [4] N. Naseri, V.Yu. Bychenkov, and W. Rozmus. Axial magnetic field generation by intense circularly polarized laser pulses in underdense plasmas. *Physics of Plasmas*, 17:083109, 2010.
- [5] T.V. Liseykina, S.V. Popruzhenko, and A. Macchi. Inverse Faraday effect driven by radiation friction. *New Journal of Physics*, 18:072001, 2016.
- [6] Z. Léczy, A. Andreev, and A. Seryi. Plasma rotation with circularly polarized laser pulse. *Laser and Particle Beams*, 34:31, 2016.
- [7] Ph. Korneev, E. d’Humières, and V. Tikhonchuk. Gigagauss-scale quasistatic magnetic field generation in a snail-shaped target. *Physical Review E*, 91:043107, 2015.
- [8] Ph. Korneev, V. Tikhonchuk, and E. d’Humières. Magnetization of laser-produced plasma in a chiral hollow target. *New Journal of Physics*, 19:033023, 2017.
- [9] S. Ali, J.R. Davies, and J.T. Mendonca. Inverse Faraday effect with linearly polarized laser pulses. *Physical Review Letters*, 105:035001, 2010.
- [10] Z. Léczy, I.V. Konoplev, A. Seryi, and A. Andreev. Gigagauss solenoidal magnetic field inside bubbles excited in under-dense plasma. *Nature:Scientific Reports*, 6:36139, 2016.
- [11] Z. Najmudin, M. Tatarakis, A. Pukhov, E.L. Clark, R.J. Clarke, A.E. Dangor, J. Faure, V. Malka, D. Neely, M.I.K. Santala, and K. Krushelnick. Measurements of the inverse Faraday effect from relativistic laser interactions with an underdense plasma. *Physical Review Letters*, 87:215004, 2001.
- [12] J. Deschamps, M. Fitaire, and M. Lagoutte. Inverse Faraday effect in a plasma. *Physical Review Letters*, 25:1330, 1970.
- [13] Y. Horovitz, S. Eliezer, A. Ludmirsky, Z. Henis, E. Moshe, R. Shpitalnik, and B. Arad. Measurements of inverse Faraday effect and absorption of circularly polarized laser light in plasmas. *Physical Review Letters*, 78:1707, 1997.
- [14] L. Allen, M.W. Beijersbergen, R.J.C. Spreeuw, and J.P. Woerdman. Orbital angular momentum of light and the transformation of Laguerre-Gaussian laser modes. *Physical Review A*, 45:8185, 1992.
- [15] W. Wang, B. Shen, X. Zhang, L. Zhang, Y. Shi, and Z. Xu. Hollow screw-like drill in plasma using an intense Laguerre-Gaussian laser. *Scientific Reports*, 5:8274, 2014.
- [16] R. Li, X. Feng, D. Zhang, K. Cui, F. Liu, and Y. Huang. Radially polarized orbital angular momentum beam emitter based on shallow-ridge silicon microring cavity. *IEEE Photonics Journal*, 6:2200710, 2014.
- [17] I. Thiele, S. Skupin, and R. Nuter. Boundary conditions for arbitrarily shaped and tightly focused laser pulses in electromagnetic codes. *Journal of Computational Physics*, 321:1110, 2016.
- [18] R. Nuter and V. T. Tikhonchuk. Prepulse suppression and optimization of backward Raman amplification with a chirped pump laser beam. *Physical Review E*, 87:043109, 2013.
- [19] J. D. Jackson. *Classical Electrodynamics*. Wiley, 1998.